

Alignment of D-state Rydberg molecules

A.T. Krupp, A. Gaj, J.B. Balewski, P. Ilzhöfer, S. Hofferberth, R. Löw, and T. Pfau
5. Physikalisches Institut, Universität Stuttgart, Pfaffenwaldring 57, 70569 Stuttgart, Germany

M. Kurz

*Zentrum für Optische Quantentechnologien, Universität Hamburg,
Luruper Chaussee 149, 22761 Hamburg, Germany*

P. Schmelcher

*Zentrum für Optische Quantentechnologien, Universität Hamburg,
Luruper Chaussee 149, 22761 Hamburg, Germany and
Hamburg Centre for Ultrafast Imaging, Universität Hamburg,
Luruper Chaussee 149, 22761 Hamburg, Germany*

(Dated: October 6, 2018)

We report on the formation of ultralong-range Rydberg D-state molecules via photoassociation in an ultracold cloud of rubidium atoms. By applying a magnetic offset field on the order of 10 G and high resolution spectroscopy, we are able to resolve individual rovibrational molecular states. A full theory, using the Born-Oppenheimer approximation including s- and p-wave scattering, reproduces the measured binding energies. The calculated molecular wavefunctions show that in the experiment we can selectively excite stationary molecular states with an extraordinary degree of alignment or anti-alignment with respect to the magnetic field axis.

Angular confinement of molecules, referred to as alignment, represents a unique way of influencing molecular motions. It is of major importance for the control of a number of molecular processes and properties, such as the pathways of chemical reactions including stereo-chemistry [1–4], photoelectron angular distributions [5–8], dissociation of molecules [9–12] and diffractive imaging of molecules [13, 14]. In the case of ultracold alkali dimers, the quantum stereodynamics of ultracold bimolecular reactions has been probed recently [15]. To achieve alignment and its ally orientation electric, magnetic and light fields, have been used in a variety of experimental configurations such as, e.g., the brute force orientation [16], hexapole focusing [17–19], strong ac pulsed fields [20] or combined ac and dc electric fields [10, 21–24]. They all have in common that they provide an angular-dependent potential energy that leads to a hybridisation of the field-free rotational motion. Beyond the above it is well-known that in strong magnetic fields the mutual orientation of the magnetic field and internuclear axis provides an intricate electronic state-dependent topology of the corresponding adiabatic potential energy surfaces (APES) yielding a plethora of equilibrium positions [25], novel bonding mechanisms [26, 27] and field-induced vibronic interactions via e.g. conical intersections of the APES [25, 28].

In the present work we show that weak magnetic fields of a dozen Gauss allow to strongly impact and control the properties of ultralong-range Rydberg molecules. Rydberg molecules have been theoretically predicted [29, 30] and experimentally observed for Rydberg S-states [31, 32] and P-states [34].

Here we investigate D-state ultralong-range rubidium Rydberg molecules for two different m_J magnetic sub-

states with high resolution spectroscopy. We can selectively excite distinct rovibrational molecular states with specific alignments and identify them by comparison of the binding energy with theoretical predictions. The bond of the ultralong-range Rydberg molecules results from the low-energy scattering between a quasi-free Rydberg electron at position \mathbf{r} and a ground state atom at \mathbf{R} . This process can be described using the Fermi pseudopotential [35], which depends on the scattering length A between two scattering partners:

$$V_{n,e}(\mathbf{r}, \mathbf{R}) = 2\pi A_s[k(\mathbf{R})]\delta(\mathbf{r} - \mathbf{R}) + 6\pi A_p^3[k(\mathbf{R})]\overleftarrow{\nabla}\delta(\mathbf{r} - \mathbf{R})\overrightarrow{\nabla}, \quad (1)$$

where $A_s(k)$ and $A_p(k)$ are the s-wave and p-wave triplet scattering lengths, respectively [36]. The momentum k of the electron can be treated in a semiclassical approximation [29]. The resulting Hamiltonian

$$H = H_0 + \frac{B}{2}(J_z + S_z) + V_{n,e}(\mathbf{r}, \mathbf{R}) + \frac{\mathbf{P}^2}{M} \quad (2)$$

consists of the field-free Hamiltonian H_0 of the Rydberg atom, the Zeeman-interaction terms of the angular momenta (spin \mathbf{S} and orbital \mathbf{L}) with the external field $\mathbf{B} = B\mathbf{e}_z$, the scattering potential (1) and the kinetic energy term. Here the total angular momentum $\mathbf{J} = \mathbf{L} + \mathbf{S}$ was introduced. We write the total wavefunction as $\Psi(\mathbf{r}, \mathbf{R}) = \psi(\mathbf{r}, \mathbf{R})\phi(\mathbf{R})$, where ψ describes the electronic molecular wavefunction in the presence of the neutral perturber for a given position \mathbf{R} and ϕ determines the rovibrational state of the perturber. The resulting APES $\epsilon(R, \Theta)$ depend on the angle of inclination Θ between the field vector and the internuclear axis as well as the internuclear distance R . By solving the Schrödinger equation in cylindrical coordinates using a

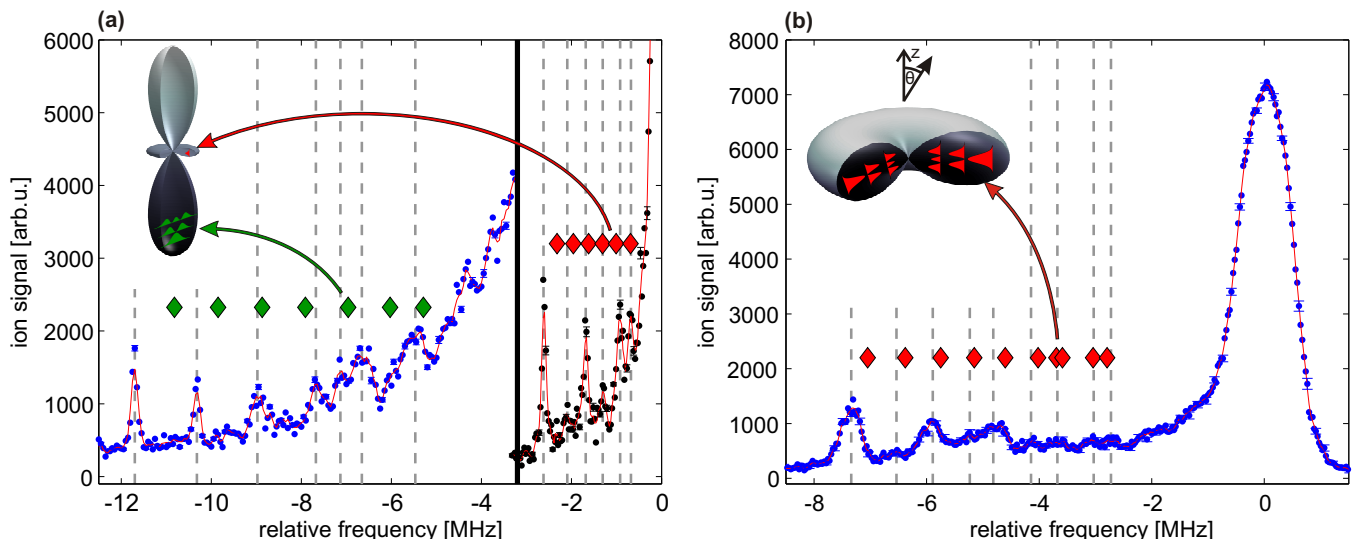


FIG. 1: Spectra of the 44D, $J=5/2$, $m_J=1/2$ (a) and 42D, $J=5/2$, $m_J=5/2$ (b) states, where the ion detector signal is plotted against the relative frequency to the atomic line. In (a) the spectrum consists of two individual spectra taken with different laser intensities separated with a black line at -3.2 MHz: the left one (blue) was taken at a high intensity to resolve the axial molecules and the right one (black) at a low intensity to decrease the power broadening of the atomic line such that we can resolve the toroidal lying molecules. For better visibility a moving average (red line) is included. To make it easier to identify the molecular positions the data was scaled by a factor of 3 for the $m_J=1/2$ state. The dashed lines (grey) mark the experimental peak positions of the molecules whereas the red and green diamonds indicate the calculated binding energies; the green diamonds were used for the axial molecules in case of $m_J=1/2$. The insets show the angular part of the electron orbitals relevant for triplet scattering. Arrows point to the positions where the molecules are created within the orbitals. The standard deviation errorbars are determined from independent measurements.

finite difference method we obtain the binding energies and molecular wavefunctions without any fitting parameters (see Supplementary Material).

In the experiment we start with an ultracold ($2 \mu\text{K}$) cloud of about $5 \cdot 10^5$ ^{87}Rb atoms in a magnetic trap (peak density $\sim 10^{13} \text{cm}^{-3}$) polarized in the $5S_{1/2}$, $F=2$, $m_F=2$ state. For the photoassociation of the molecules, a σ^+ -polarized laser at 780 nm, 500 MHz detuned from the intermediate $5P_{3/2}$ state, and a laser at 480 nm (combined laser linewidth $< 30 \text{kHz}$) are used. A magnetic field of $B=13.55 \text{G}$ is applied to separate the different atomic m_J states, leading to a Zeeman splitting of the fine structure states of $\sim 22 \text{MHz}$. After the $50 \mu\text{s}$ long Rydberg excitation pulse we field-ionize the Rydberg states and accelerate the ions towards a microchannel plate detector. In a single cloud we perform up to 400 cycles of excitation and detection while scanning the laser frequency. This permits us to take one spectrum within a minute. More information about the experimental setup can be found in [37]. We investigate the stretched state $J=5/2$, $m_J=5/2$ and the $J=5/2$, $m_J=1/2$ state. To address only these states we change the polarization of the 480 nm laser to either σ^+ ($m_J=5/2$) or σ^- ($m_J=1/2$). For principal quantum numbers n ranging from 41 to 49 the total angular momentum quantum number J is still a good quantum number since the fine structure splitting of ~ 170 to 98MHz (for $n=41$ to 49) is large compared to the Zeeman splitting. This region was chosen as for lower

quantum numbers $n < 40$ the binding energies of the outermost molecular states are on the same energy scale as the Zeeman splitting. This would lead to an undesired overlap of the molecular states with the neighboring atomic line. For higher principal quantum numbers $n > 50$ the distance between neighboring molecular lines decreases below our spectral resolution [38].

Photoassociation spectra of the 44D, $J=5/2$, $m_J=1/2$ and 42D, $J=5/2$, $m_J=5/2$ states are shown in Fig.1 (a) and (b), respectively. The confinement of the electron density in the polar coordinate Θ leads to a large number of excited rovibrational states visible in the spectrum in contrast to previous S-state measurements [31, 32]. This causes stationary molecular states featuring different degrees of alignment.

For the $m_J=5/2$ state (Fig.1 (b)), the molecular states are anti-aligned in a plane perpendicular to the quantization axis, at $\Theta = \pi/2$. The molecular potential at this position is $|Y_{l=2}^{m=2}(\Theta = \pi/2)|^2 / |Y_{l=0}^{m=0}|^2 = 1.875$ times deeper than in the well known Rydberg S-state molecules. This factor explains well the measured binding energies of the deepest bound states. In addition the energies of the excited rovibrational states are reproduced by our calculations indicated as red diamonds. For the $m_J=1/2$ state two classes of molecular states appear, one localized in the polar lobes ($\Theta = 0, \pi$; green) and the other one in the toroidal part of the orbital in the equatorial plane ($\Theta = \pi/2$; red). The angular part of the molecu-

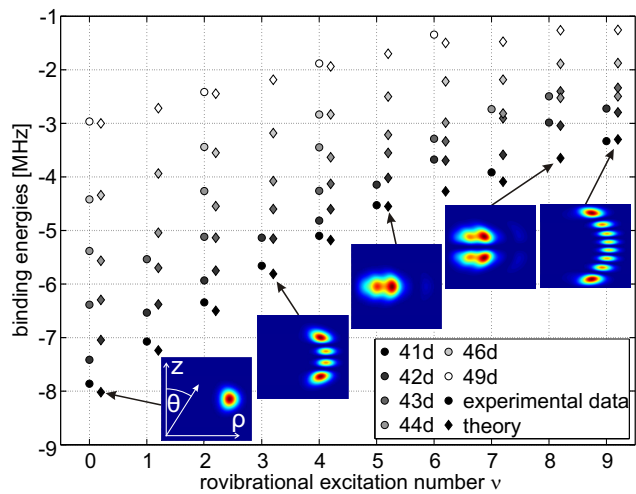


FIG. 2: Molecular binding energies for the $m_J=5/2$ states plotted against the rovibrational excitation numbers ν for principal quantum numbers n ranging from 41 to 49. For increasing n the states are colored brighter. The calculated binding energies (diamonds) are plotted with a horizontal offset to the experimental ones (circles) to improve readability. The insets depict the probability densities ranging from $\rho=2000a_0$ to $\rho=3300a_0$ and for $z=-1500a_0$ to $z=1500a_0$ of certain rovibrational states.

lar potential of the $m_J=1/2$ state including the Clebsch-Gordan coefficient scales as $3/5 \cdot |Y_{l=2}^{m=0}(\Theta)|^2$. Note that this state is a superposition of a singlet and triplet state, where we can neglect the singlet part due to its small scattering length [39]. As a result the lowest aligned axial molecular state shows a binding energy four times larger than the one for the anti-aligned toroidal case and three times larger than for the corresponding S-state molecules. Both estimates are in good agreement with the experimental results. The calculated binding energies of the excited states are indicated by red and green diamonds in Fig.1(a). The difference in strength of the two classes of molecular states can be attributed to the different spatial extent of the potential wells leading to larger Franck-Condon factors for the anti-aligned toroidal states. The agreement of the measured binding energies with the results of our calculations over a wide range of principal quantum numbers is most evident in Fig.5 and Fig.6. It is worth to mention that the energy of rotation and vibration are of the same order of magnitude; thus the spectroscopic lines cannot be assigned to rotational and vibrational states separately and only one rovibrational quantum number ν is used. From the volume of the Rydberg atom, one obtains a scaling of the potential depth with the effective principal quantum number as n^{*-6} . The binding energy, however, also depends on the shape of the potential, so that the scaling law does not describe our high resolution data sufficiently.

All in all, the full calculation of the binding energies fit the experimental $m_J=5/2$ state data (Fig.5) and the $m_J=1/2$ data for the toroidal molecules (Fig.6(b)) well.

In the insets of Fig.5 and Fig.6 the probability densities of specific rovibrational states in z and ρ -direction are shown. From these color plots, the variable degree of the alignment, defined as $\langle \cos^2(\Theta) \rangle$, becomes obvious. Starting from the ground state $\nu=0$, the molecular wavefunction begins to spread in Θ -direction until it extends to the first radial excitation at $\nu=6$, valid for all n and m_J . In the case of the 42D, $m_J=1/2$ state we obtain an alignment of 0.01 of the toroidal ground state which increases with rovibrational excitation number. For the axial case we get alignments starting from 0.98 decreasing with increasing higher axial excitation numbers.

In conclusion, we report on the observation of D-state ultralong-range Rydberg molecules exposed to magnetic fields in high resolution spectroscopy. The maximally stretched $m_J=5/2$ and the $m_J=1/2$ Rydberg states lead, due to their different electronic configurations, to adiabatic potential energy surfaces with different topologies. For $m_J=5/2$ the two-dimensional potential landscape $\epsilon(R, \Theta)$ possesses a series of local wells located at $\Theta = \pi/2$ which lead to anti-aligned rovibrational states leaving their signatures in a series of peaks of the spectroscopic detection of the ultralong-range Rydberg molecules. On the contrary the $m_J=1/2$ potential surfaces exhibit a number of radial wells at $\Theta = 0, \pi$ and a series of weaker potential wells for $\Theta = \pi/2$. The latter are caused by the axial and toroidal character of the corresponding electronic configuration and lead to aligned and anti-aligned rovibrational states. Spectroscopically these are observed as a sequence of peaks far off and close by to the main atomic Rydberg transition, respectively. A change of the principal quantum number n introduces only quantitative changes to the above picture where theory and experiment show a good agreement. This work opens the doorway to the control of Rydberg molecular structures and even chemical reaction dynamics by external fields. For polyatomic states, i.e. several neutral perturbers, it can be conjectured that magnetic and/or electric fields can be used to strongly change the molecular geometry for weak field strengths which is otherwise impossible both for ground state molecules and also for the traditional molecular Rydberg states containing a tight molecular positively charged core. Even more, the design of conical intersections [28, 40] yielding ultrafast decay or predissociation processes along selected chemical reaction coordinates comes into the reach of experimental progress in the field of ultracold molecular physics.

During the finalization of this manuscript we became aware of related work [41].

Acknowledgments

This work is funded by the Deutsche Forschungsgemeinschaft (DFG) within the SFB/TRR21 and the project PF 381/4-2. We also acknowledge support by the ERC under contract number 267100 and from E.U. Marie

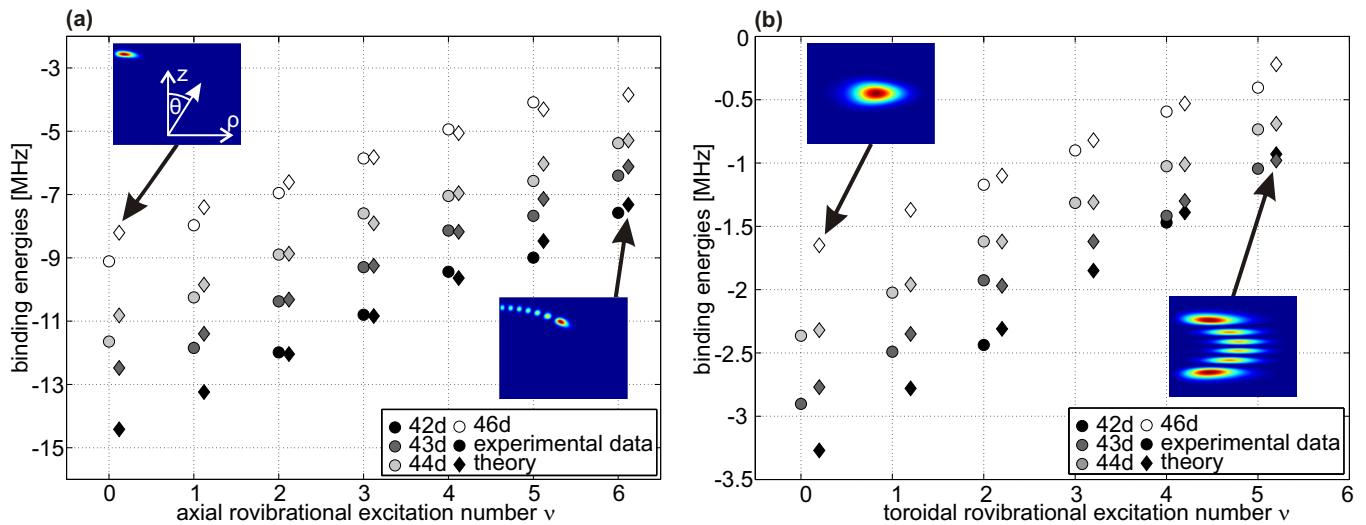


FIG. 3: Molecular binding energies for the $m_J=1/2$ states plotted against the axial rovibrational excitation numbers (a) and the toroidal rovibrational excitation numbers (b), respectively, for principal quantum numbers n ranging from 42 to 46. For increasing n the states are colored brighter. The calculated binding energies (diamonds) are plotted with a horizontal offset to the experimental ones (circles) to improve readability. The insets depict the probability densities in z - and ρ -direction of selected rovibrational states. For the axial rovibrational excitation numbers (a) ρ ranges from 0 to $3500a_0$ and z from 0 to $3500a_0$ whereas the toroidal rovibrational excitation numbers range from (b) $\rho=2700a_0$ to $3500a_0$ and $z=-2250a_0$ to $2250a_0$ (further details can be found in the supplementary material).

Curie program ITN-Coherence 265031. P.S. acknowledges financial support by the Deutsche Forschungsgemeinschaft (DFG) through the excellence cluster The

Hamburg Centre for Ultrafast Imaging - Structure, Dynamics, and Control of Matter on the Atomic Scale.

-
- [1] P. R. Brooks and E. M. Jones, *J. Chem. Phys.* **45**, 3449 (1966).
- [2] S. Stolte, *Ber. Bunsen. Phys. Chem.* **86**, 413 (1982).
- [3] R. Zare, *Science* **20**, 1875 (1998).
- [4] V. Aquilanti, M. Bartolomei, F. Pirani, D. Cappelletti, and F. Vecchiocattivi, *Phys. Chem. Chem. Phys.* **7**, 291 (2005).
- [5] L. Holmegaard, J. L. Hansen, L. Kalhøj, S. L. Kragh, H. Stapelfeldt, F. Filsinger, J. Küpper, G. Meijer, D. Dimitrovski, M. Abu-samha, C. P. J. Martiny, and L. B. Madsen, *Nat. Phys.* **6**, 428 (2010).
- [6] J. L. Hansen, L. Holmegaard, L. Kalhøj, S. L. Kragh, H. Stapelfeldt, F. Filsinger, G. Meijer, J. Küpper, D. Dimitrovski, M. Abu-samha, C. P. J. Martiny, and L. B. Madsen, *Phys. Rev. A* **83**, 023406 (2011).
- [7] A. Landers, T. Weber, I. Ali, A. Cassimi, M. Hattass, O. Jagutzki, A. Nauert, T. Osipov, A. Staudte, M. Prior, H. Schmidt-Böcking, C. Cocke, and R. Dörner, *Phys. Rev. Lett.* **87**, 013002 (2001).
- [8] C. Z. Bisgaard, O. J. Clarkin, G. R. Wu, A. M. D. Lee, C. Gessner, C. C. Hayden, and A. Stolow, *Science* **323**, 1464 (2009).
- [9] M. Wu, R. J. Bemish, and R. E. Miller, *J. Chem. Phys.* **101**, 9447 (1994).
- [10] R. Baumfalk, N. H. Nahler, and U. Buck, *J. Chem. Phys.* **114**, 4755 (2001).
- [11] A. J. van den Brom, T. P. Rakitzis, and M. H. M. Janssen, *J. Chem. Phys.* **121**, 11645 (2004).
- [12] M. L. Lipciuc, A. J. van den Brom, L. Dinu, and M. H. M. Janssen, *Rev. Sci. Instrum.* **76**, 123103 (2005).
- [13] J. C. H. Spence and R. B. Doak, *Phys. Rev. Lett.* **92**, 198102 (2004).
- [14] F. Filsinger, G. Meijer, H. Stapelfeldt, H. Chapman, and J. Küpper, *Phys. Chem. Chem. Phys.* **13**, 2076 (2011).
- [15] M. H. G. de Miranda, A. Chotia, B. Neyenhuis, D. Wang, G. Quémener, S. Ospelkaus, J. L. Bohn, J. Ye, and D. S. Jin, *Nature Physics* (2011).
- [16] H. J. Loesch and A. Remscheid, *J. Chem. Phys.* **93**, 4779 (1990).
- [17] P. R. Brooks, *Science* **193**, 11 (1976).
- [18] D. H. Parker and R. B. Bernstein, *Annu. Rev. Phys. Chem.* **40**, 561 (1989).
- [19] T. D. Hain, R. M. Moision, and T. J. Curtiss, *J. Chem. Phys.* **111**, 6797 (1999).
- [20] H. Stapelfeldt and T. Seideman, *Rev. Mod. Phys.* **75**, 543 (2003).
- [21] B. Friedrich and D. R. Herschbach, *J. Chem. Phys.* **111**, 6157 (1999).
- [22] B. Friedrich and D. R. Herschbach, *J. Phys. Chem. A* **103**, 10280 (1999).
- [23] H. Sakai, S. Minemoto, H. Nanjo, H. Tanji, and T. Suzuki, *Phys. Rev. Lett.* **90**, 083001 (2003).
- [24] H. Tanji, S. Minemoto, and H. Sakai, *Phys. Rev. A* **72**, 063401 (2005).
- [25] U. Kappes and P. Schmelcher, *Phys. Lett. A* **210**, 409 (1996); *Phys. Rev. A* **53**, 3869 (1996).

- [26] T. Detmer, P. Schmelcher and L.S. Cederbaum, *Phys. Rev. A* **57**, 1767 (1998); *Atoms and Molecules in Strong External Fields*, Editors: P. Schmelcher and W. Schweizer, **Plenum Publishing Company** 1998.
- [27] K. K. Lange, E. I. Tellgren, M. R. Hoffmann, and T. Helgaker, *Science* **337**, 327 (2012).
- [28] P. Schmelcher and L. S. Cederbaum, *Phys. Rev. A* **41**, 4936 (1990).
- [29] C. H. Greene, A. S. Dickinson, and H. R. Sadeghpour, *Phys. Rev. Lett.* **85**, 2458 (2000).
- [30] I. Lesanovsky, P. Schmelcher, and H. R. Sadeghpour, *Journal of Physics B: Atomic, Molecular and Optical Physics* **39**, L69 (2006).
- [31] V. Bendkowsky, B. Butscher, J. Nipper, J. P. Shaffer, R. Löw, and T. Pfau, *Nature* **458**, 0028 (2009).
- [32] V. Bendkowsky, B. Butscher, J. Nipper, J. B. Balewski, J. P. Shaffer, R. Löw, T. Pfau, W. Li, J. Stanojevic, T. Pohl, and J. M. Rost, *Phys. Rev. Lett.* **105**, 163201 (2010).
- [33] J. Tallant, S. T. Rittenhouse, D. Booth, H. R. Sadeghpour, and J. P. Shaffer, *Phys. Rev. Lett.* **109**, 173202 (2012).
- [34] M. A. Bellos, R. Carollo, J. Banerjee, E. E. Eyler, P. L. Gould, and W. C. Stwalley, *Phys. Rev. Lett.* **111**, 053001 (2013).
- [35] E. Fermi, *Nuovo Cimento* **11**, 157 (1934).
- [36] A. Omont, *J. Phys. France* **38**, 1343 (1977).
- [37] R. Löw, H. Weimer, J. Nipper, J. B. Balewski, B. Butscher, H. P. Büchler, and T. Pfau, *J. Phys. B: At. Mol. Opt. Phys.* **45**, 113001 (2012).
- [38] J. B. Balewski, A. T. Krupp, A. Gaj, D. Peter, H. P. Büchler, R. Löw, S. Hofferberth, and T. Pfau, *Nature* **502**, 664 (2013).
- [39] C. Bahrim, U. Thumm, and I. I. Fabrikant, *J. Phys. B: At. Mol. Opt. Phys.* **34**, L195 (2001).
- [40] M. Mayle, S. T. Rittenhouse, P. Schmelcher, and H. R. Sadeghpour, *Phys. Rev. A* **85**, 052511 (2012).
- [41] D. A. Anderson, S. A. Miller and G. Raithel, arXiv:1401.2477.

I. SUPPLEMENTARY MATERIAL

A. Molecular Hamiltonian in a magnetic field

We consider a highly excited Rydberg atom interacting with a ground state neutral perturber atom (we will focus on the ^{87}Rb atom here) in a static and homogeneous magnetic field. The Hamiltonian treating the Rb ionic core and the neutral perturber as point particles is given by

$$H = \frac{\mathbf{P}^2}{M} + H_{\text{el}} + V_{\text{n,e}}(\mathbf{r}, \mathbf{R}), \quad (3)$$

$$H_{\text{el}} = H_0 + \frac{1}{2}\mathbf{B}(\mathbf{L} + 2\mathbf{S}) + \frac{1}{8}(\mathbf{B} \times \mathbf{r})^2, \quad (4)$$

where $(M, \mathbf{P}, \mathbf{R})$ denote the atomic Rb mass and the relative momentum and position of the neutral perturber with respect to the ionic core. The vector \mathbf{r} indicates the relative position of the Rydberg electron to the ionic core. The electronic Hamiltonian H_{el} consists of the field-free Hamiltonian H_0 of the Rydberg atom and the usual paramagnetic and diamagnetic terms of an electron in a static external magnetic field. The Hamiltonian H_0 includes the Rydberg quantum defects due to electron-core scattering and the fine structure. H_{el} contains also the Zeeman-interaction terms of the angular momenta (spin and orbital) with the external field. We choose $\mathbf{B} = B\mathbf{e}_z$. The interatomic potential $V_{\text{n,e}}$ for the low-energy scattering between the Rydberg electron and the neutral perturber is described as a Fermi-pseudopotential

$$V_{\text{n,e}}(\mathbf{r}, \mathbf{R}) = 2\pi A_s[k(R)]\delta(\mathbf{r} - \mathbf{R}) + 6\pi A_p^3[k(R)]\overleftarrow{\nabla}\delta(\mathbf{r} - \mathbf{R})\overrightarrow{\nabla}. \quad (5)$$

Here we consider the triplet scattering of the electron from the ground state alkali atom. $A_s(k) = -\tan[\delta_0(k)]/k$ and $A_p^3(k) = -\tan[\delta_1(k)]/k^3$ denote the energy-dependent triplet s - and p -wave scattering lengths. $\delta_{l=0,1}(k)$ are the energy dependent phase shifts (see Fig. (4)). The wave vector $k(R)$ is determined by the semiclassical relation $k(R)^2/2 = E_{\text{kin}} = -1/2n^2 + 1/R$ [29, 36].

We introduce the total angular momentum $\mathbf{J} = \mathbf{L} + \mathbf{S}$ and write the total wave function as $\Psi(\mathbf{r}, \mathbf{R}) = \psi(\mathbf{r}; \mathbf{R})\phi(\mathbf{R})$. Within the adiabatic approximation we obtain

$$[H_0 + \frac{B}{2}(J_z + S_z) + \frac{B^2}{8}(x^2 + y^2) + V_{\text{n,e}}(\mathbf{r}, \mathbf{R})]\psi_{n,m_J}(\mathbf{r}; \mathbf{R}) = \epsilon_{n,m_J}(\mathbf{R})\psi_{n,m_J}(\mathbf{r}; \mathbf{R}), \quad (6)$$

$$\left(\frac{\mathbf{P}^2}{M} + \epsilon_{n,m_J}(\mathbf{R})\right)\phi_{\nu m}^{(n,m_J)}(\mathbf{R}) = E_{\nu m}^{(n,m_J)}\phi_{\nu m}^{(n,m_J)}(\mathbf{R}), \quad (7)$$

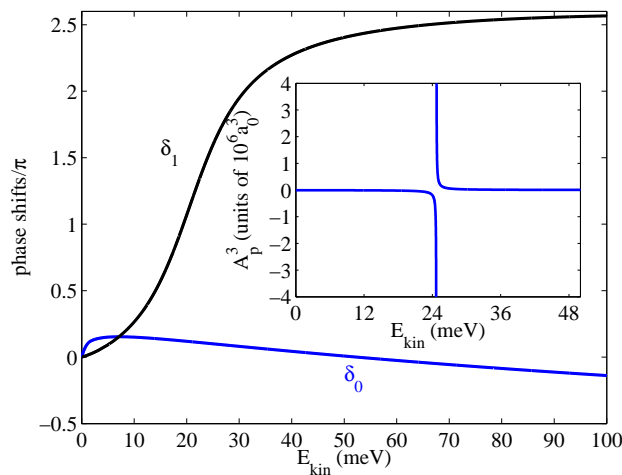


FIG. 4: Energy dependent triplet phase shifts δ_1 and δ_0 for $e^{-87}\text{Rb}(5s)$ scattering. For $E_{\text{kin}} = 24.7\text{meV}$ the phase shift $\delta_1 = \pi/2$, i.e. the (cubed) energy dependent p -wave scattering length $A_p^3(k) = -\tan(\delta_1(k))/k^3$ possesses a resonance at this energy. This can be clearly seen in the inset.

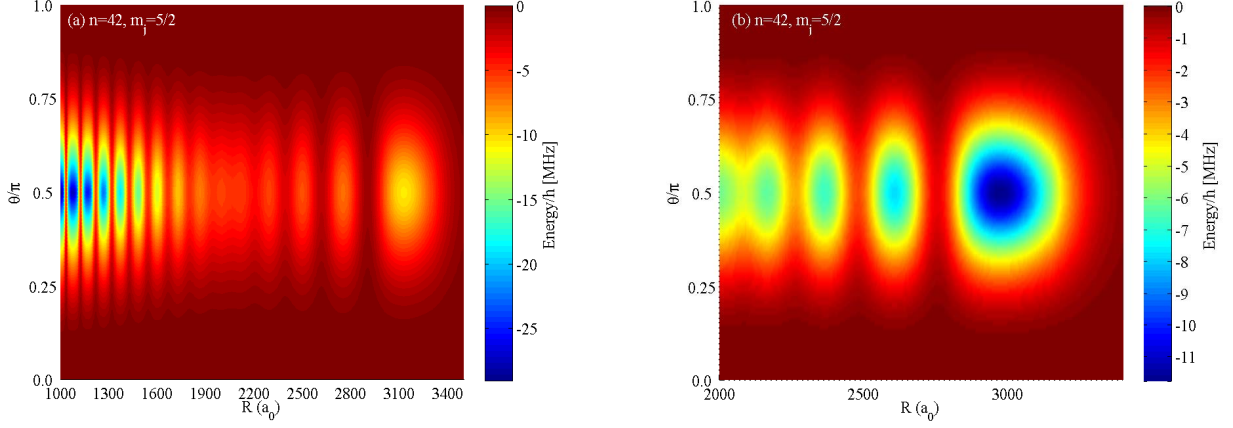


FIG. 5: (a) $42D_{5/2}, m_J = 5/2$ APES as a function of (R, θ) for $1000a_0 \leq R \leq 3400a_0$. One can clearly identify a local potential minimum at $\theta = \pi/2$, $R \approx 3100a_0$ with a depth of around 12MHz and several neighboring wells with decreasing depths. For $R \leq 2000a_0$ the APES possesses a strongly oscillatory structure with a series of local potential minima increasing in depth. These oscillations are caused by the increasing impact of the p -wave scattering term which possesses a resonance at $R_{\text{res}} \approx 800a_0$. Figure (b) shows the same APES but in the range $2000a_0 \leq R \leq 3400a_0$

where ψ_{n,m_J} describes the electronic molecular wave function in the presence of the neutral perturber for a given relative position \mathbf{R} and $\phi_{\nu m}^{(n,m_J)}$ determines the rovibrational state of the perturber.

In this work a field strength of $B = 13.55G$ is chosen. For such a field strength the diamagnetic term in (6) can be neglected. Furthermore, the adiabatic potential energy surfaces (APES) $\epsilon_{\nu m_J}(\mathbf{R})$ possesses rotational symmetry around the z -axis, which means they depend on the angle of inclination θ between the field vector and the internuclear axis, e. g., $\epsilon_{n,m_J}(\mathbf{R}) = \epsilon_{n,m_J}(R, \theta)$. In case we use cylindrical coordinates, the APES are functions of (z, ρ) .

B. Basis set

We calculate the APES for the $n = 42, 43, 44, 46, 49$, $J = 5/2$, $m_J = 1/2$ and $n = 41, 42, 43, 44, 46, 49$, $J = 5/2$, $m_J = 5/2$ fine structure states. The spin orbit coupling causes a level splitting between the $J = 3/2, 5/2$ states in the range of 170MHz ($n = 41$) to 98MHz ($n = 49$). To obtain the potential curves we have performed a diagonalization of the electronic Hamiltonian (6) using the eigenstates $|n, J = l \pm 1/2, m_J, l = 2, s = \frac{1}{2}\rangle$ of H_0 with

$$\begin{aligned} & \langle \mathbf{r} | n, J = l \pm \frac{1}{2}, m_J, 2, \frac{1}{2} \rangle \\ &= R_{n,j,2}(r) \left(\pm \sqrt{\frac{\frac{5}{2} \pm m_J}{5}} Y_{2,m_J-1/2}(\theta, \phi) | \uparrow \rangle + \sqrt{\frac{\frac{5}{2} \mp m_J}{5}} Y_{2,m_J+1/2}(\theta, \phi) | \downarrow \rangle \right) \\ &\equiv R_{n,j,2}(r) (\alpha(j, m_J) Y_{2,m_J-1/2}(\theta, \phi) | \uparrow \rangle + \beta(j, m_J) Y_{2,m_J+1/2}(\theta, \phi) | \downarrow \rangle) \end{aligned}$$

$Y_{lm}(\theta, \phi)$ are the spherical harmonics.

C. Potential energy surfaces

We obtain APES with different topologies depending on the level of electronic excitation (Fig. (5)-(6)). The characteristic features of the $n = 42$, $m_J = 1/2, 5/2$ potential surface which we present in Fig. (5)-(6) remain up to the $n = 49$ APES.

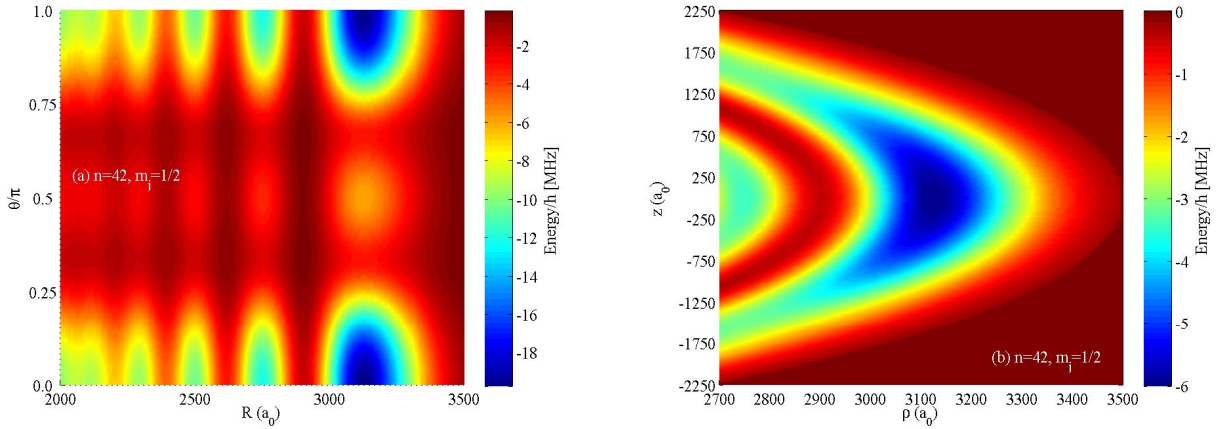


FIG. 6: (a) $42D_{5/2}, m_J = 1/2$ APES as a function of (R, θ) for $2000a_0 \leq R \leq 3500a_0$. We clearly see two potential wells at $\theta = 0, \pi$; $R \approx 3150a_0$ with a depth of 20MHz. In addition, a more shallow well with a depth of 6MHz can be identified at $\theta = \pi/2$, $R \approx 3150a_0$. With decreasing R neighboring potential wells decrease in depths. Figure (b) shows the vicinity of the shallow potential well in cylindrical coordinates.

D. Rovibrational levels and binding energies

For the rovibrational wavefunctions we choose the following ansatz

$$\phi_{\nu m}^{(n, m_J)}(\mathbf{R}) = \frac{F_{\nu m}^{(n, m_J)}(\rho, z)}{\sqrt{\rho}} \exp(im\varphi), \quad m \in \mathbb{Z}, \nu \in \mathbb{N}_0. \quad (8)$$

With this we can write the rovibrational Hamiltonian as

$$H_{\text{rv}} = -\frac{1}{M}(\partial_\rho^2 + \partial_z^2) + \frac{m^2 - 1/4}{M\rho^2} + \epsilon_{n, m_J}(\rho, z). \quad (9)$$

We solve this differential equation using a finite difference method. For a fixed m we label the eigenenergies with $\nu = 0, 1, 2, \dots$ and define the binding energy $E_B^{(\nu)}$ of an eigenstate as the absolute value between the eigenenergy and the dissociation limit of the APES. Because $\epsilon_{n, m_J}(\rho, -z) = \epsilon_{n, m_J}(\rho, z)$ the functions $F_{\nu m}^{(n, m_J)}$ fulfill $F_{\nu m}^{(n, m_J)}(\rho, -z) = \pm F_{\nu m}^{(n, m_J)}(\rho, z)$, which means $|F_{\nu m}^{(n, m_J)}(\rho, -z)|^2 = |F_{\nu m}^{(n, m_J)}(\rho, z)|^2$ for the probability density.

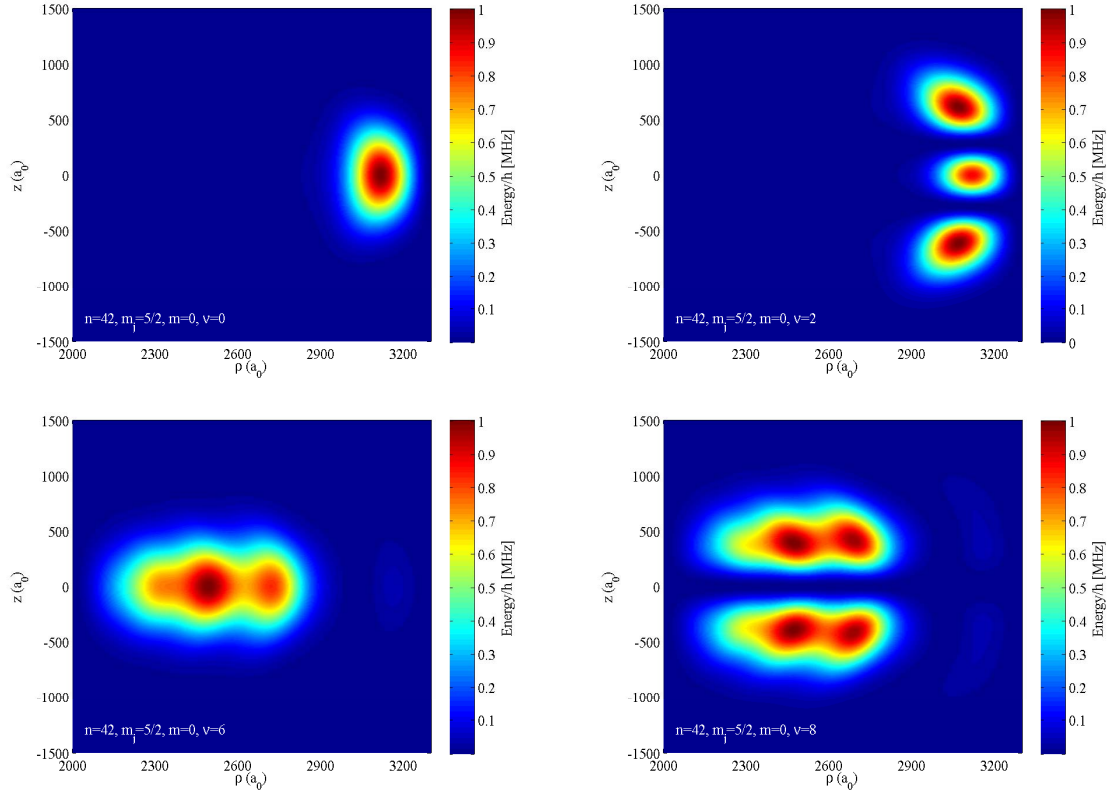


FIG. 7: (Scaled) rovibrational probability densities $|F_{\nu 0}(\rho, z)|^2$ for $42D_{5/2}$, $m_J = 5/2$ APES.

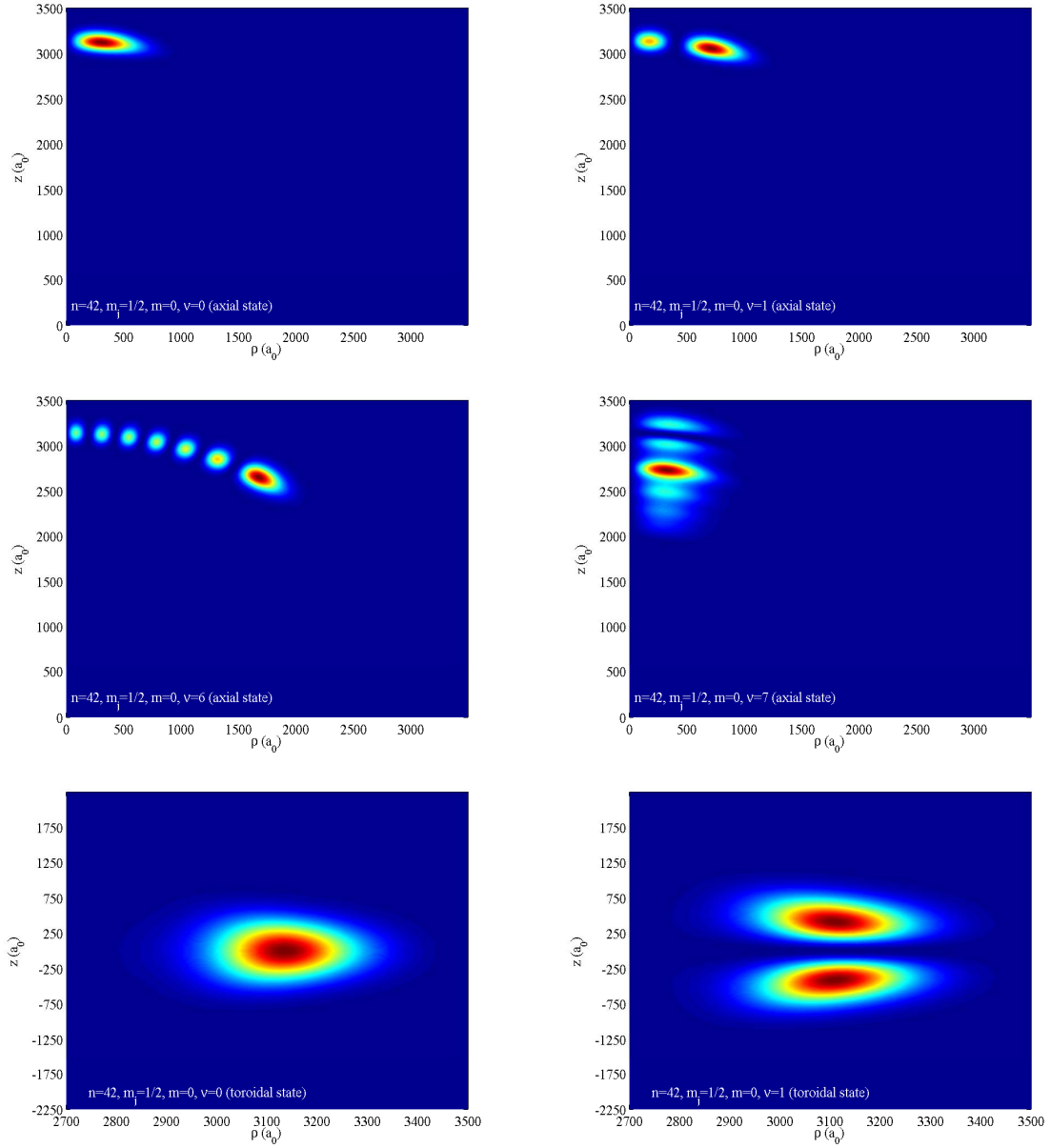


FIG. 8: (Scaled) probability densities $|F_{\nu 0}(\rho, z)|^2$ for $42D_{5/2}$, $m_J = 1/2$ APES. We distinguish between axial ($\theta = 0, \pi$) and toroidal states ($\theta = \pi/2$).